Numerical research on kerf characteristics of abrasive waterjet machining based on the SPH-DEM-FEM approach

Mingming Du[1,2] · Haijin Wang[1,2] 🅾 · Huiyue Dong[1,2] · Yingjie Guo[1,2] · Yinglin Ke[1,2]

Abstract

Abrasive waterjet machining has been widely used because of flexibility, but the cutting accuracy is difficult to ensure due to the lack of dynamic analysis in the forming process of the kerf. In this paper, a coupled SPH-DEM-FEM method is proposed to predict the cutting qualities of the abrasive water jet machining under different process parameters and reveal the mechanism of the kerf formation. Compared with previous simulation methods, the new simulation method has advantages in the simulations for long-term water jet cutting. The abrasive particles and waterjet particles are continuously generated during calculations to reduce the model size and raise the calculation efficiency. The discrete element method (DEM) is utilized to characterize the flow of abrasive particles, which follows the Gaussian distribution. The collisions of non-spherical particles are concerned by the friction factors. The water flow with large deformation is expressed in the smoothed particle hydrodynamics (SPH) method. And the erosion contact is set between particles and the target. Finally, experiments are conducted to verify the authenticity of the simulation model. The cutting depths and kerf top widths obtained by the simulations are consistent with the experimental results.

1 Introduction

As an alternative non-conventional machining process for difficult-to-cut materials, abrasive waterjet (AWJ) machining has received critical attention with the advantages of no thermal distortion, low cutting forces, and high machining versatility [1, 2]. Thus, it has been widely used in various industries, including the mechanical precision component, intelligent automotive engineering, and aerospace equipment, where the machining performance with high accuracy and quality is required [3, 4]. As a critical factor affecting its application, the characteristics of kerf have been particularly concerned [5]. Various research methods, such as experimental analysis [6, 7], theoretical modeling [8, 9],

and numerical simulation [10, 11], are applied to study the performance of AWJ machining. Nevertheless, the numerical method has attracted increasing attention because of its efficiency and rationality recently.

In order to understand the mechanism of AWJ machining in-depth, a great deal of numerical simulation research has investigated the flow characteristics inside the nozzle [12, 13], the external flow distribution [14, 15], and the impacted topography of the target [10, 16–19]. The impacted target models could be generally divided into two categories, namely single particle impact effect and multiple particles overlapping footprints. In practice, the individual abrasive impact models with different geometries and various impingement angles are often used to study the erosion wear mechanism during AWJ machining [10, 16]. These models need to be extended into multiple particles impact situations to imitate a more realistic AWJ machining case.

Besides, there are various simulation methods utilized in AWJ simulations. Computational fluid dynamics (CFD) are commonly adopted in AWJ simulations to investigate the dynamic characteristics of waterjet. Nyaboro et al. [14] studied the machined surface contour by using the CFD-erosion approach. Wenjun et al. [20] presented a finite element (FE) model for the AWJ machining process by arbitrary

✉ Haijin Wang
wo1004@163.com

1   State Key Laboratory of Fluid Power and Mechatronic Systems, College of Mechanical Engineering, Zhejiang University, Hangzhou 310027, China

2   Key Laboratory of Advanced Manufacturing Technology of Zhejiang Province, College of Mechanical Engineering, Zhejiang University, Hangzhou 310027, China

Lagrange-Euler (ALE) method, which predefined abrasive particles and water mixing in an element. Finite element analysis is also a widely used approach to study the erosion wear by abrasive particle impacts at high velocity. Anwar et al. [17, 21] established an AWJ milling FE model and correctly selected the shapes, size distribution, and velocities of abrasive particles. But the water effect was ignored. Lozano Torrubia et al. [22] pointed out the importance of inherent fluctuations in the AWJ machining process. Therefore, they combined the Monte Carlo methods into the FE model to study the footprint variability. The smoothed particle hydrodynamics (SPH) is a meshfree, Lagrangian particle method that is capable of modeling fluid flows robustly. So, it is widely used in modeling the AWJ machining process. Jianming et al. [18] firstly created a column of SPH particles defining in water material and then changed the properties of some particles to represent abrasive particles randomly. Also, the size of abrasive particles is equivalent to the average diameter offered by the supporters. Xiangwei et al. [23] modeled the garnet abrasive particles as arbitrarily shaped rigid bodies by SPH and conducted the material removal simulations of continuous abrasive-jet flow to demonstrate the ability of this new model over previous models. But Jingxiao et al. [24] pointed out that the smoothed quantities of particles may show falsified values when densities and masses of neighboring particles vary mainly within the smooth length.

Although the existing simulation models have studied the influence of process parameters on the AWJ cutting qualities, the research about the cutting attributes of the water jet is lacking. Thus, the primary goal of this paper is to investigate the mechanism of kerf formation for thick plates by the coupled SPH-DEM-FEM method. In this method, the discrete element method (DEM) is firstly applied to represent the continuous abrasive particle flow, in which the abrasive parameters such as abrasive particle size distribution, abrasive mass flow rate, and abrasive materials are concerned. The water flow is modeled by the SPH method with the enhanced fluid formulation, and the workpiece is modeled by FE incorporating the material failure response. Furthermore, the multi-physics problems as fluid-structure interaction and fluid dynamics are solved on LS-DYNA.

The main contribution of this paper is to predict the kerf profiles with reasonable accuracy at various process parameters. For the first time, the numerical model revealed the formation mechanism of the kerfs and clarified that the material removal rate in the center of the jet is low because of the existence of the stagnation zone. In contrast, the material removal rate at the edge of the jet is high during the machining process. The remainder of this article is structured as follows. Section 2 describes the basic theory of the coupled DEM-SPH-FEM method. In Section 3, the modeling procedure is introduced. In Section 4, the applicability of the model is verified by comparing the analytical results with the experimental data. In Section 5, the predicted effects of different process parameters as abrasive mass flow rates, abrasive particle sizes, and impingement angles are demonstrated. Finally, the article is concluded in Section 6.

2 The basic theory of coupled SPH-DEM-FEM approach

2.1 SPH fluid-phase model

In the SPH algorithm, a set of arbitrarily distributed particles is used to represent the problem domain. Field function is characterized by the superposition of the corresponding values of the particles in a local domain. Compared with the FE method, the SPH method does not need to mesh the target in advance. It is capable of solving complex problems such as high-speed impact, massive material distortion, and free-surface flow.

The formulations of the SPH method are divided into two key steps. The first step is the kernel estimation, which converts the partial differential equation of the field variables into the form of continuous integral functions, and the second is particle approximation, which represents the integral functions by the sum of discrete ordinary differential equations, as given in Eq. (1). Then, the value of any field variable $f(x_i)$ at particle i can be obtained by weighted superposition of the field variable values corresponding to all particles in the support domain, as illustrated in Fig. 1.

$$f(x_i) = \sum_{j=1}^{N} \frac{m_j}{\rho_j} f(x_j) W(|x_i - x_j|, h) \tag{1}$$

where the letters i and j are particles; N is the total number of all particles in the support domain with a radius of $2h$; m_j and ρ_j are the mass and density at particle j.

The spatial derivative of function $f(x_i)$ can be calculated by $\nabla f(x)$ as

$$\langle \nabla f(x_i) \rangle = -\sum_{j=1}^{N} \frac{m_j}{\rho_j} f(x_j) \cdot \nabla W_{ij}$$
$$\text{with} \nabla W_{ij} = \nabla W \frac{x_j - x_i}{h} \tag{2}$$

where ∇W_{ij} is the gradient of the kernel function associated with particle j at particle i. Therefore, the continuity equation of motion and the conservation equation of momentum and energy can be written in the SPH form as

$$\begin{cases} \dfrac{d\rho_i}{dt} = \sum_{j=1}^{N} m_j f(x_j) \nabla W_{ij} \\ \dfrac{dv_i}{dt} = -\sum_{j=1}^{N} m_j \left(\dfrac{p_i}{\rho_i^2} + \dfrac{p_j}{\rho_j^2} + \Pi_{ij} \right) \nabla W_{ij} \\ \dfrac{de_i}{dt} = \dfrac{1}{2} \sum_{j=1}^{N} m_j \left(\dfrac{p_i}{\rho_i^2} + \dfrac{p_j}{\rho_j^2} + \Pi_{ij} \right) v_{ij} * \nabla W_{ij} \end{cases} \tag{3}$$
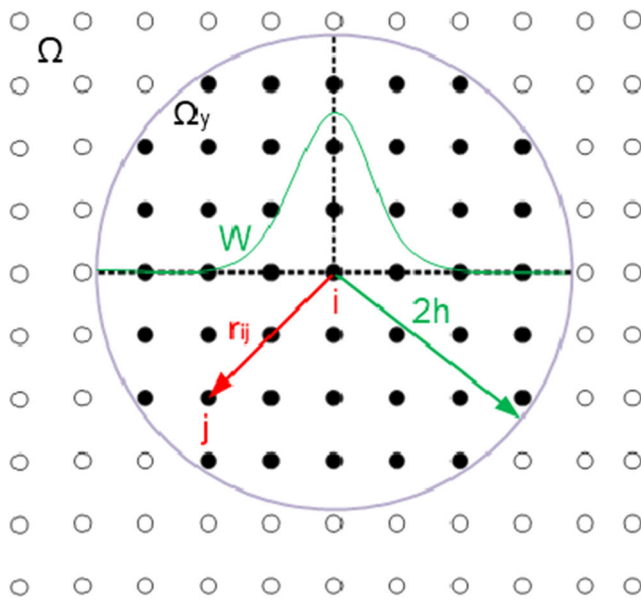
- **Support domain of smoothing function for particle i , Ω$_y$**
- **Integration domain, Ω**
- **Smoothing function, W**
- **Smoothing length, 2h**

Fig. 1 SPH particle support domain

where p_i is stress tensor, v_i is the velocity, and $\prod_{ij}$ is the artificial viscosity term, which is shown as

$$\prod_{ij} = \begin{cases} \dfrac{-Q_2 \overline{c}_{ij} \mu_{ij} + Q_1 \mu_{ij}^2}{\overline{\rho}_{ij}} & \text{if } v_{ij}*x_{ij} < 0 \\ 0 & \text{if } v_{ij}*x_{ij} \geq 0 \end{cases} \quad (4)$$

with $v_{ij} = v_i - v_j, x_{ij} = x_i - x_j, \mu_{ij} = \dfrac{h_{ij}*v_{ij}*x_{ij}}{|x_{ij}|^2 + 0.01h_{ij}}$

where $h_{ij} = (h_i - h_j)/2$, and Q_1 and Q_2 are user-defined parameters. Besides, to make the SPH particles column behaves more realistic like the jet plume of AWJ machining, an enhanced fluid formulation [25] is recommended in the simulation model.

2.2 DEM granular flow model

The DEM is a particle-based numerical method that has been extensively used to study the granular media, e.g., sand and rocks [26, 27]. This method, in which the discrete elements are modeled as rigid spherical particles, solves Newton's equation of motion to track the positions, velocities, and accelerations of each particle individually. Given DEM particle i with the initial position x_i, the equation of motion is expressed as

Fig. 2 DEM particle collision contact
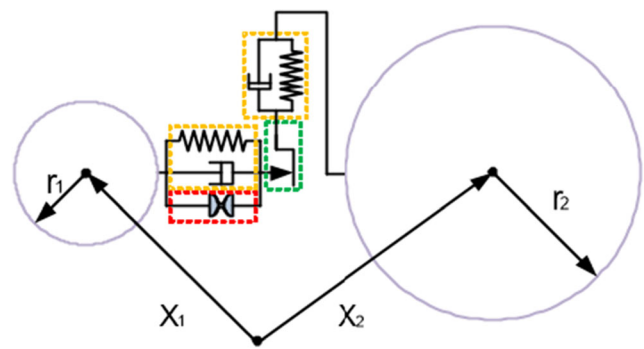
- ● **Friction parameters**
- ● **Contact damping and stiffness**
- ● **Capilarry forces parameters**

$$\begin{cases} m_i \dfrac{\mathrm{d}^2 x_i}{\mathrm{d}t^2} = \sum_j c_{ij} + f_i + m_i g \\ I_i \dfrac{\mathrm{d}^2 \phi_i}{\mathrm{d}t^2} = \sum_j M_{ij} \end{cases} \quad (5)$$

where m_i is the mass of particle i; c_{ij} denotes interaction force between particle i and j; M_{ij} is the moment of particle j to i; f_i represents drag force of water flow to DEM particle i. The DEM inter-particle collision contact can be calculated using a spring damping model [28], including elastic force, damping force, friction force, and capillary force between micro-particles, as shown in Fig. 2.

3 Numerical modeling method

3.1 Material modeling

3.1.1 Waterjet material model

Waterjet is modeled based on SPH formulations. The NULL material model, coupled with the Murnaghan equation-of-state (EOS), is used to describe the behavior of water [29]. The Murnaghan is a newly developed keyword for SPH fluid flow modeling in LS-DYNA, in which a density re-initialization scheme is adopted to overcome the pressure

Table 1 Material parameters of water [30, 31]

Description	Parameters
Mass density	998.2 (kg/m^3)
Dynamic viscosity	1.02×10^{-3} (Pa s)
Cut-off pressure	-1.0×1020 (Pa)
Bulk modulus	2.22×109 (Pa)

Table 2 EOS parameters of water [30, 31]

Equation of state	Murnaghan	
GAMMA	K0	V0
7	8.0213×10^9	0

oscillation issue. This EOS modeling weakly compressible fluid flow by SPH methods expresses as

$$p = k_0 \left[\left(\frac{\rho}{\rho_0} \right)^\gamma - 1 \right] \qquad (6)$$

where p is the pressure at any point in the fluid; ρ_0 is the density of water at rest; γ is a standard constant generally set to 7, and k_0 can be selected by

$$k_0 \geq \frac{100 \rho_0 v_{\max}^2}{\gamma} \qquad (7)$$

where $v_{\max}$ is the maximum expected fluid flow velocity, which is set 750 m/s as the maximum water pressure is 360 MPa in the model. Table 1 shows the material model parameters for water.

Table 2 shows the EOS parameters for water.

3.1.2 Abrasive particles material model

The DEM algorithm is adopted to characterize the behavior of discrete particle flow in this paper. In the AWJ machining operations, the abrasives are usually selected from materials with high rigidity and hardness such as garnet and brown corundum, and the deformation of abrasives is neglected when compared to targets. Thus, the rigid material model is chosen for abrasives modeling, where the grains interact by automatic single surface contact definition. Almandine garnet sand was selected as the material of the abrasive particles in the experiments. The material model parameters are shown in Table 3.

3.1.3 Workpiece material model

In a high-rate impact situation, the commonly used model for the dynamic plastic deformation of ductile materials is Johnson and Cook model [32], which consists of the plasticity model and the failure model. The Johnson-Cook plasticity model is applied to characterize the relationship of plastic flow stress on the effective plastic strain, effective strain rate, and temperature as

Table 3 Material parameters of abrasive particles [17]

Description	Parameters
Size	80 mesh
Mass density	4120 (kg/m^3)
Young's modulus	248 (GPa)
Poisson's ratio	0.3

Table 4 Material parameters of the workpiece [33]

Description	Parameters
Mass density	7.85×10^3 (kg/m^3)
Young's modulus	207 (GPa)
Shear modulus	770 (GPa)
Poisson's ratio	0.32
Melt temperature	1793 (K)

$$\sigma_y = \left(A + B\overline{\varepsilon}^{p^n} \right) \left(1 + c\ln\dot{\varepsilon}^* \right) \left(1 - T^{*m} \right)$$
$$\text{with}$$
$$\dot{\varepsilon}^* = \begin{cases} \dfrac{\dot{\overline{\varepsilon}}}{\text{EPSO}} & \text{for VP} = 0 \\[2mm] \dfrac{\dot{\overline{\varepsilon}}^p}{\text{EPSO}} & \text{for VP} = 1 \end{cases} \qquad (8)$$

where A, B, c, n, and m are input constants, $\overline{\varepsilon}^p$ is the effective plastic strain, $\dot{\overline{\varepsilon}}$ is the effective total strain, and $\dot{\varepsilon}^*$ is the normalized effective strain rate, and T^* is the homologous temperature. In general, the viscoplastic strain rate formulation (VP = 1) is recommended in modeling since the standard strain rate formulation (VP = 0) often produces noisy effective strain rates [29]. The accumulation of plastic strain is included in the Johnson-Cook failure model as

$$\varepsilon^f = \max\left(\left[D_1 + D_2 \exp D_3 \sigma^* \right] \left[1 + D_4 \ln \dot{\varepsilon}^* \right] \left[1 + D_5 T^* \right], \text{EFMIN} \right)$$
$$\text{with } \sigma^* = \frac{p}{\sigma_{\text{eff}}} \qquad (9)$$

where D_1 to D_5 stands for the material constants and σ^* is the ratio of pressure p divided by effective stress σ_{eff}. The Johnson-Cook material constants for C45 are detailed in Table 4.

The parameters of the Johnson-Cook plasticity model and the Johnson-Cook failure model are shown in Table 5.

In this model, the Gruneisen EOS [29] with cubic shock velocity as the function of particle velocity $v_{s.}$ (v_p) is selected to define the pressure for compressed materials as

$$p = \frac{\rho_0 C^2 \mu \left[1 + \left(1 - \frac{\gamma_0}{2} \right) \mu - \frac{a}{2} \mu^2 \right]}{\left[1 - (S_1 - 1)\mu - S_2 \frac{\mu^2}{\mu+1} - S_3 \frac{\mu^3}{(\mu+1)^2} \right]} + (\gamma_0 + a\mu) E a$$
$$\text{with } \mu = \frac{\rho}{\rho_0} - 1 \qquad (10)$$

Table 5 The Johnson-Cook material parameters of the workpiece [33]

Material model type				Johnson-Cook					
A	B	c	n	m	D$_1$	D$_2$	D$_3$	D$_4$	D$_5$
792	510	0.260	0.014	1.03	5	0	0	0	0

Table 6   EOS parameters of the workpiece

Equation of state				Gruneisen	
C/(m/s)	S_1	S_2	S_3	γ_0	a
4569	1.49	0	0	2.17	0.43

where C is the intercept of the v_s (v_p) curve; S_1, S_2, and S_3 are the coefficients of the slope of the v_s (v_p) curve; γ_0 is the Gruneisen gamma; a is the first-order volume correction to γ_0 (Table 6).

3.2 Meshfree particle generation and FE meshing

3.2.1 SPH particle generation

The automatic particle generation method is adopted in this paper by specifying the particle injection time and velocity, which dramatically reduces the complexity of the modeling process and saves calculation resources. The waterjet is injected from the nozzle outlet area, as illustrated in Fig. 3. The number of SPH particles is determined by the injection volume.

3.2.2 DEM particle generation

Similarly, the discrete elements are initially injected from the nozzle area along with SPH particles. The DEM particles are generated at the center area of the injection source region and follow the Gaussian distribution, as shown in Fig. 4. The number of DEM particles is related to the injection mass and particle sizes. There are 672 DEM particles and 96,834 SPH particles generated in 300 μs when the mass flow rate of abrasives is 0.18 kg/min. More particles can be produced by extending the injection time or increasing the mass flow rate needless remodeling operations. Besides, the contact parameters such as the
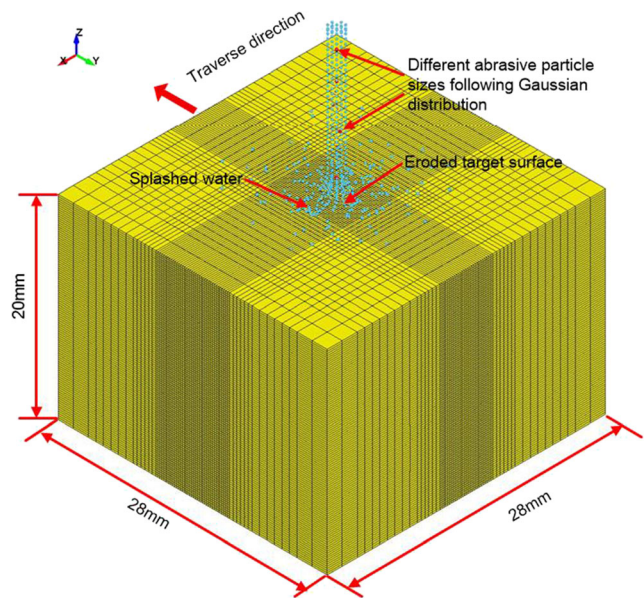

Fig. 4   Abrasive particles spatial distribution in the simulation model

static coefficient of friction, the rolling friction coefficient, and the capillary forces between particles are defined to characterize the irregular abrasive particle behavior.

3.2.3 FE mesh density

The size of the geometric model for the workpiece is a cuboid of size 25 mm × 25 mm × 20 mm. In order to improve the computational efficiency while ensuring the accuracy of the calculation results, a more refined mesh is used in the center of the sample, and a relatively coarser mesh is employed in the outer region, as illustrated in Fig. 4. All the elements in the refined mesh region are the same size of 0.125 mm. It is worth
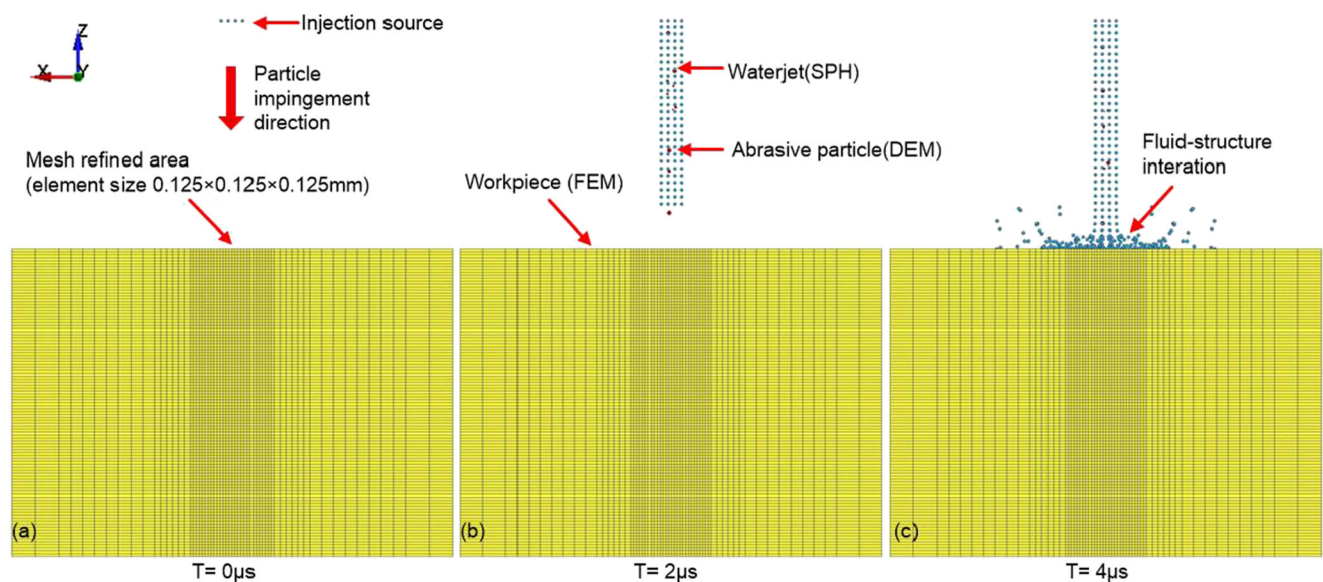

Fig. 3   SPH-DEM-FEM model for AWJ machining

noting that hourglass energy is an essential factor affecting the accuracy of calculation results [29]. Thus, the 8-node hexahedron set 1-point solid element is implemented in the current model. Hourglass type 10 is based on a total strain formulation, which provides high accuracy and insignificant mesh sensitivity. Besides, the ratio of hourglass energy to the total energy should be checked when the calculation is completed. If the ratio exceeds 10%, which implies the element distortion is too large, the relative parameters need to be re-adjusted.

3.3 Initial and boundary conditions

3.3.1 The initial velocity of the abrasive water jet

The flow field in the orifice can be regarded as a constant flow of the one-dimensional fluid which generates high-speed water jet. The initial velocity of the pure water jet can be calculated by Bernoulli's law [34]. Considering the momentum losses owing to the frictional resistance of sidewalls, the fluid-flow disturbances, and the compressibility of water, the correct velocity of the water flow can be calculated by

$$v_w = \kappa \sqrt{\frac{2P_i}{\rho_w}} \tag{11}$$

where the water pressure P_i is selected by the typical operating pressure for ultrahigh-pressure AWJ machining applications; ρ_w is the water flow density; κ is the efficiency coefficient. According to the experimental research work of Momber [34], the typical value for κ based on jet-force measurements is $0.83 < \kappa < 0.93$.

Due to the influence of the mixing process with abrasive particles inside the mixing chamber and the focusing tube, the velocity of the abrasive waterjet at the nozzle outlet can be calculated by the momentum exchange formula. The momentum transfer efficiency of abrasive particles mixed with the waterjet is usually taken as the value from 0.73 to 0.94 [35]. Thus, the calculation formula of the real dynamic velocity of the abrasive waterjet at the outlet of nozzle is expressed as

$$v_a = \frac{\chi v_w}{1 + \dot{m}_a / \dot{m}_w} \tag{12}$$

where $\dot{m}_w$ and $\dot{m}_a$ are water mass flow rate and abrasive mass flow rate, respectively; χ is the efficiency coefficient. It is

apparent that the velocity of the abrasive particle is slower than that of the abrasive particles after escaping from the nozzle. Thus, the contact between abrasive particles and waterjet is considered by defining the contact between DEM and SPH particles.

3.3.2 Boundary conditions

In order to support the workpiece, the bottom surface of the target model is constrained in the X and Z directions, and the workpiece is set to move in the Y-direction. At the same time, the jet beam is fixed to simulate a continuous AWJ machining process. Besides, the surrounding surfaces of the workpiece are set as the non-reflection boundary to exclude the effects of stress wave reflection. Therefore, the upper face on which high-speed particles impact the workpiece is a free surface.

3.4 Contact description

3.4.1 Particle to particle contact

The interaction between particles can be divided into three groups, namely SPH to SPH particle contact, DEM to DEM particle contact, and SPH to DEM particle contact.
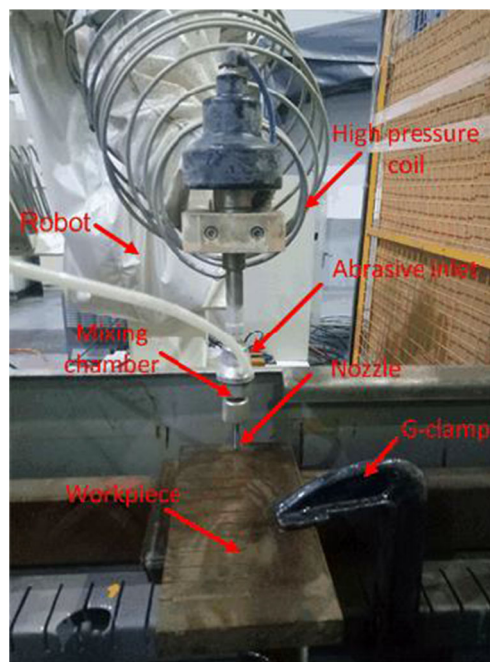
Table 7 Parameters in particle to particle contact [28]

Description	Parameters
P-P friction coefficient	0.57
P-P rolling friction coefficient	0.01
CAP	1
GAMMA	7.20×10^{-8} (GPa)

Table 8 Parameters in abrasive particle to structure contact [26]

Description	Parameters
P-W friction coefficient	0.3
P-W rolling friction coefficient	0.01
Damping coefficient	0.8

Fig. 5 Photograph of the experimental setup

Table 9 Operation parameters in the AWJ cutting experiments

Parameters	Description
Water pressure	200, 240, 280, 320, 360 (MPa)
Traverse speed	80, 120, 160, 200, 240 (mm/min)
Standoff distance	2 (mm)
Abrasive mass flow rate	0.18 (kg/min)
Jet impact angle	90°

The SPH to SPH particle contact represents the water self-interaction. And the abrasive particle collisions can be modeled as DEM to DEM particles in touch with each other. The penalty-based particle to particle interaction is realized by defining normal and tangential stiffness, damping coefficients, static, and rolling friction coefficients. These parameters play an important role in controlling the discrete sphere particles acting in a non-spherical way. It is also one of the advantages of using the DEM method to simulate abrasive particles. As the abrasive particles could be regarded as a kind of granular sand, the present model uses the wet sand frictional parameters as an approximation, which is presented in Table 7. The CAP is one of the DEM particle contact parameters defined to express the capillary force between abrasive particles.
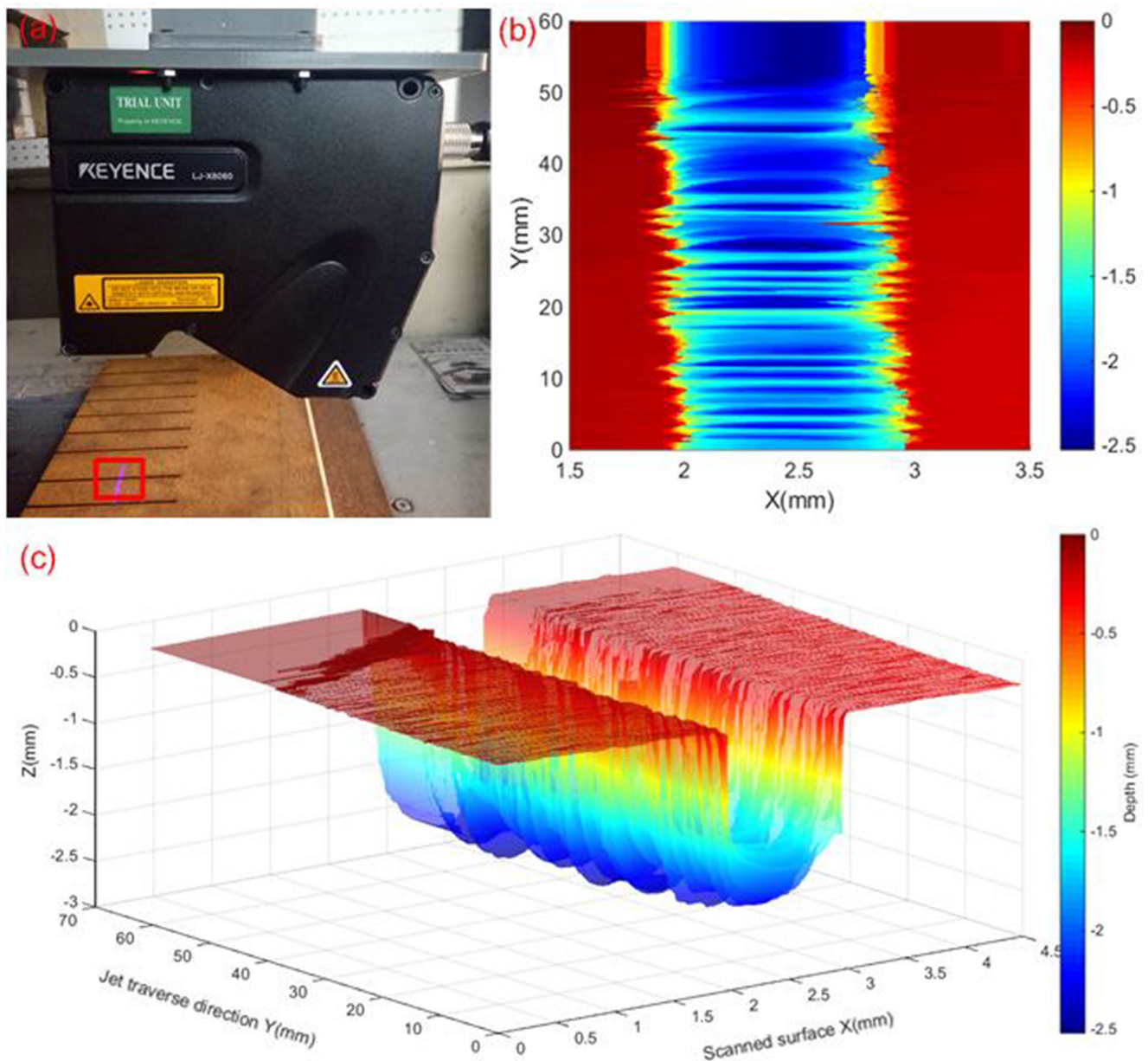
Fig. 6 Measurements of the experimental cutting kerfs. **a** The measuring instruments. **b** 2D-scanned surface. **c** 3D-scanned surface
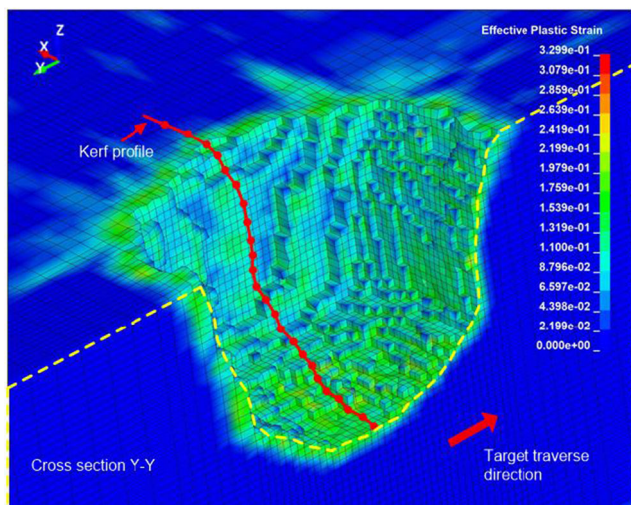
Fig. 7 Outputs in the centric cross-section Y-Y view of the FEM workpiece under the impact of abrasive waterjet

3.4.2 Particle to structure contact

The particle-structure contact refers to interactions of waterjet and abrasive particles to the workpiece. The SPH particles connected with the FEM structures could be defined by the penalty-based node to surface contact, where the slave part is the SPH node-set, and the master part is the FEM faces of the workpiece. As for the coupling method of the DEM particles and the FEM structures, a non-tied coupling interface between particles and the surface is implemented, which controls the spherical discrete elements acting like non-spherical abrasive particles. The parameters friction and damping parameters in this keyword are defined according to Table 8.

4 Experimental verification

4.1 Experimental design

The verification experiments were performed on a KMT waterjet cutting system, as shown in Fig. 5. This platform was equipped with a streamline waterjet intensifier high output pump (KMT SL-VI 50), which provided water pressure up to 413.7 MPa (60,000 psi) and was based on a 6-axis robot (Fanuc M20IA). The speed of the robot end-effector varied from 1 to 120,000 mm/min, and the repeat positioning accuracy was ± 0.05 mm. For all the trails, the abrasive nozzle assembly parameters were kept constant as standard configurations, i.e., the orifice diameter (0.33 mm), the nozzle diameter (1.02 mm), and the nozzle length (76.2 mm).

The specimens were C45 plates with 200 mm × 100 mm × 20 mm dimensional sizes. The abrasive was 80 mesh almandine garnet sand, which was the most commonly used in the abrasive waterjet machining process. Besides, an automatic abrasive metering system was used to ensure the accurate control of the abrasive mass flow rate throughout the experiments.

Full factorial experiments were designed to verify the accuracy of the numerical simulation. The length of each slit was 60 mm, and the cutting parameters could be referred to in Table 9. In the experiments, appropriate water pressure was considered at a 2-mm standoff distance between the nozzle and the specimen, while the abrasive mass flow rate was kept constant at 0.18 kg/min. Furthermore, five levels of the traverse speed and water pressure were selected within the equipment limitations and the typical ranges of AWJ machining.
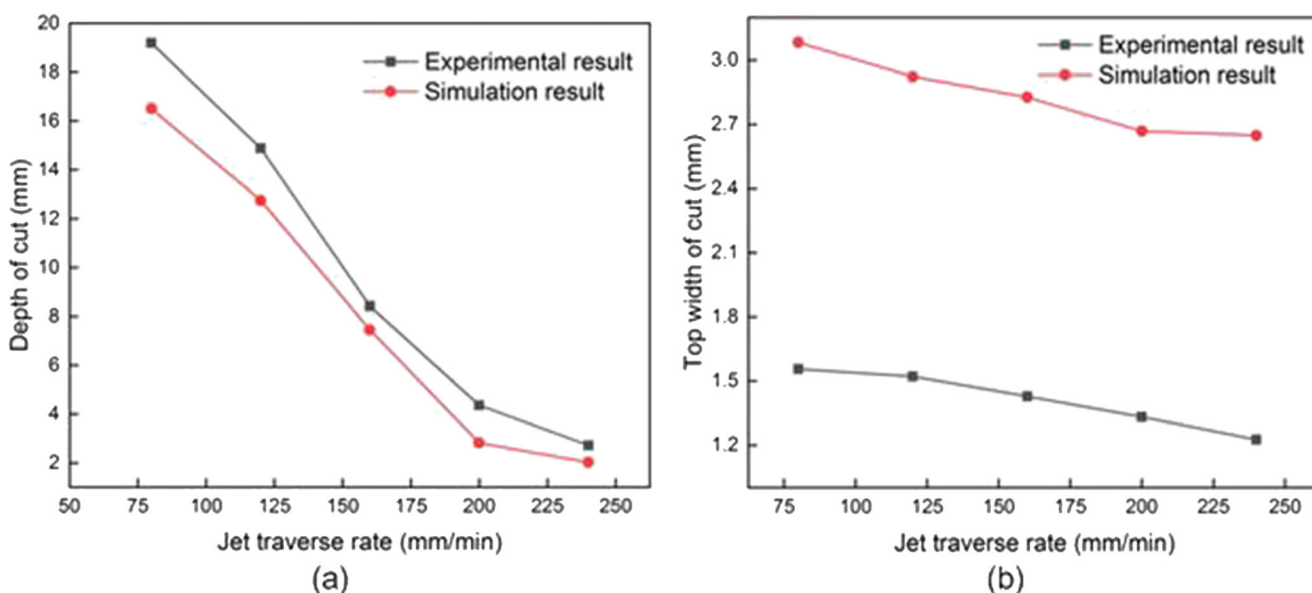

(a)

(b)

Fig. 8 Experimental and simulation results of AWJ cutting depth and width under different traverse speeds: **a** depth of cut; **b** top width of cut

Besides, all trails were at a 90° impact angle on the 20 mm specimens, and special cares were taken to the nozzle to eliminate the effect of nozzle wear on cutting performance.

4.2 Comparison between model-predicted and experimental results

Once the AWJ cutting finished, the kerf profiles were measured by the 3D Laser Profiler (KEYENCE LJ-X8060), which enabled a resolution of 0.005 mm in X-axis, 0.0412 mm in Y-axis, and 0.0146 mm in Z-axis. The scanned area is 4.5 mm in width and 60 mm along the jet traverse direction. In order to ensure the accuracy of the measured cutting profiles, the average value of the measurement results was taken as the record of the cutting depth, kerf top and bottom widths the corresponding parameter. When the depth of the kerf exceeds the measurement range of the sensor, the contour line of the end face is considered to be the profile of the entire trench. The numerical modeling results can be verified by comparing the simulated kerf depth with the corresponding experimental results (Fig. 6).

The simulation and experimental results of the AWJ cutting process under different traverse speeds and water pressures were compared. Firstly, the average velocity of the water flow and abrasive particles were calculated according to the actual water pressure used in the experiments by Eqs. (11) and (12). Secondly, the workpiece was set to move in the opposite direction of traverse speed, and abrasive waterjet was fixed in the simulation model according to the principles of motion relativity. Finally,

the cutting depths under different traverse speeds and water pressures were calculated, as shown in Fig. 7.

The compared results of different traverse speeds are shown in Fig. 8a. It is reflected that the total cutting depth decreases almost linearly with the traverse speed. However, the decrease rate declines when the speed reaches a certain level. The simulated AWJ cutting depths are consistent with the experimental results, while the errors are under 15%. The fair agreements confirm the effectiveness of the simulation model, which can be implanted for process control as well as optimization of operating parameters.

Although the depths of the simulated results are in good agreement with the experimental results as traverse speed changes, there are more differences in the top width of the kerf, as depicted in Fig. 8b. The predicted kerf top width error is about 40%. It is because that the proposed model in the paper is unable to consider the effect of standoff distance on the AWJ cutting characteristics, which has an essential influence on the profile, as pointed out by Chen et al. [36]. Thus, the whole-stage AWJ simulation model, including the internal and external flow fields of abrasive waterjet, needs to be established in recent research, improving prediction accuracy. Besides, the error value changes 0.161 mm in total, which is very little. Therefore, it can be concluded that the kerf width simulation results can predict the changing trend of the kerf top width.

The validity of the model is further verified by the water pressure of the abrasive waterjet machining, as shown in Fig. 9. It can be seen from Fig. 9a that the kerf depth increases with water pressure almost linear at the initial stage, but the rate drops as the water pressure further rises. It may be due to the fact that more energy is allocated to expand the kerf width, as
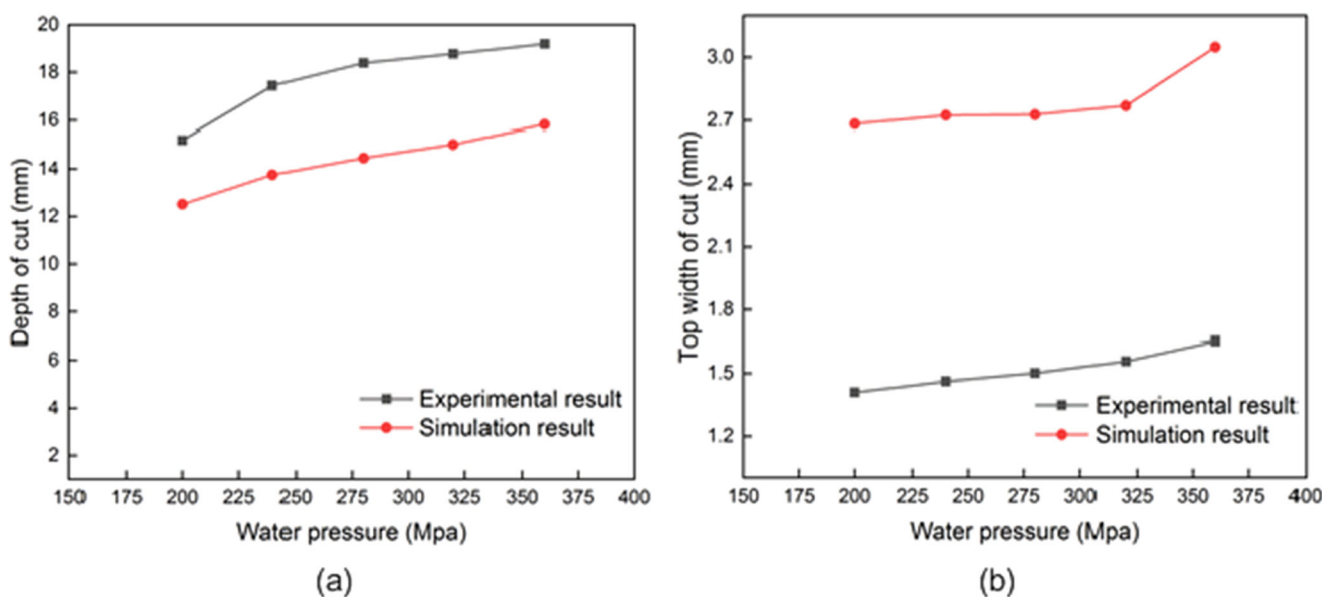

Fig. 9 Experimental and simulation results of AWJ cutting depths and width under different water pressure

shown in Fig. 9b. The top width of the kerf increases with the increase in water pressure. Thus, the conclusions can be drawn from Fig. 9 that the simulation results are in good agreement with the experimental data.

5 Results and discussion

5.1 The mechanism of kerf formation

It is of great significance to study the kerf formation process and geometric characteristics for better control of the AWJ machining process. But at present, there is no measurement method available to observe the evolution process directly unless a reliable AWJ simulation model is used. In Fig. 10, the kerf formation process due to the high-speed impacts of abrasive particles on the target surface is illustrated. It can be seen that the top width and depth of cutting increase with time, and the profile stabilizes until the jet passes by.

Figure 11 presents a typical AWJ eroded surface from the simulations. It can be concluded from Fig. 11b that the pressure distribution is not uniform in different impacted areas. The closer to the central square, the lower the pressure value is. Besides, the material removal rate follows the same rule. The periphery of the jet removes the material faster, but the central area cannot remove the content effectively. The reason for this difference can be explained by the trajectory of water flow and abrasive particles in Fig. 11a. When the jet beam initially impacts the target, the periphery of the jet expands faster than the release wave generated by the hydraulic shock. Thus, a shock front is formed inside the waterjet. The shock front propagates and finally reaches a quasi-steady state when the abrasive particles are entrained into the jet, and the material begins to be removed. This area is named the pressure stagnation zone in the middle part of the waterjet. Also, the stress of the abrasive water jet impacting the surface of the target is a ring-shaped distribution, which means that the pressure in the central area is low, and the stress value at the edge is high. Similar results have been discovered by Schwartzentruber et al. when AWJ piercing composites [37].

The phenomenon of low material removal rate in the center of the jet was also verified by experiments, as shown in Fig. 12. When the jet impacts the workpiece for a short period of time, craters are generated. The depth of the bottom center of crater is shallower than that of the side as shown in Fig. 12b. The material in crater center is not removed because of the presence of the pressure stagnation zone.

Furthermore, the material is piled up at the boundaries of the simulated kerfs, as depicted in Fig. 13. This is due
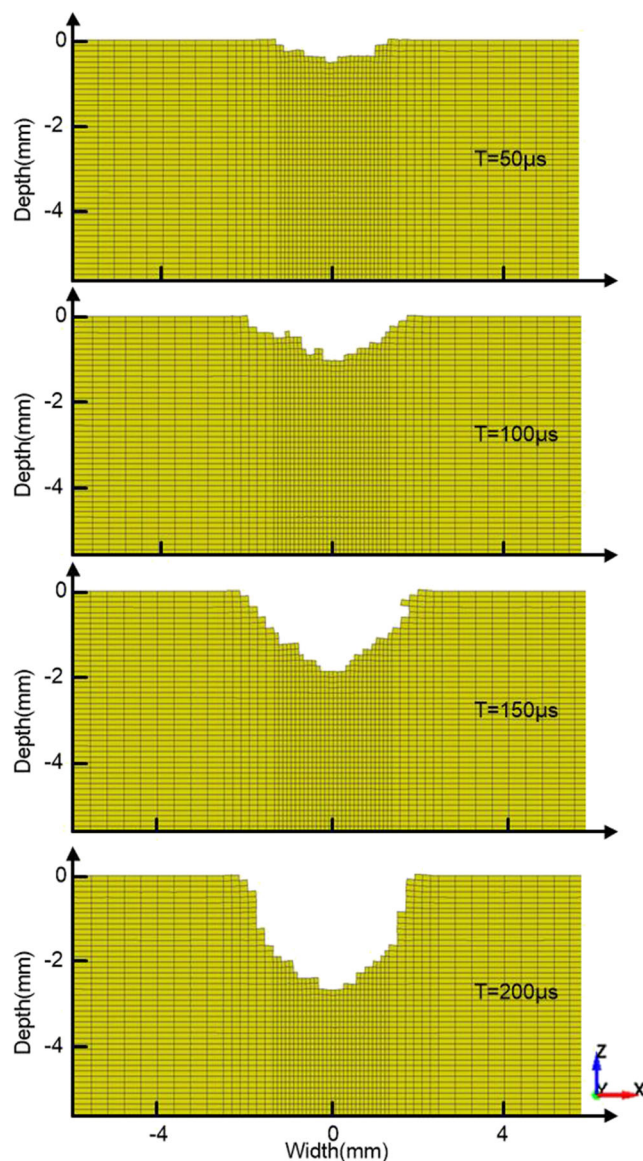

Fig. 10 Simulation results in the centric cross-section X-X view for AWJ cutting depth at different stages

to the fact that the abrasive particles may impact the target surface vertically at the first strike. But more oblique impacts will occur on the newly formed kerf walls when the secondary or third impacts happened. Anwar et al. also pointed out that the abrasive particles randomly distributed in the jet beam strike the surface both inside and outside. Thus, the width of the footprints varied across the jet traverse direction [17].

5.2 The effect of abrasive parameters

In this paper, the improved AWJ modeling method uses DEM to characterize the abrasive particle flow, which makes the abrasive parameters such as abrasive mass flow
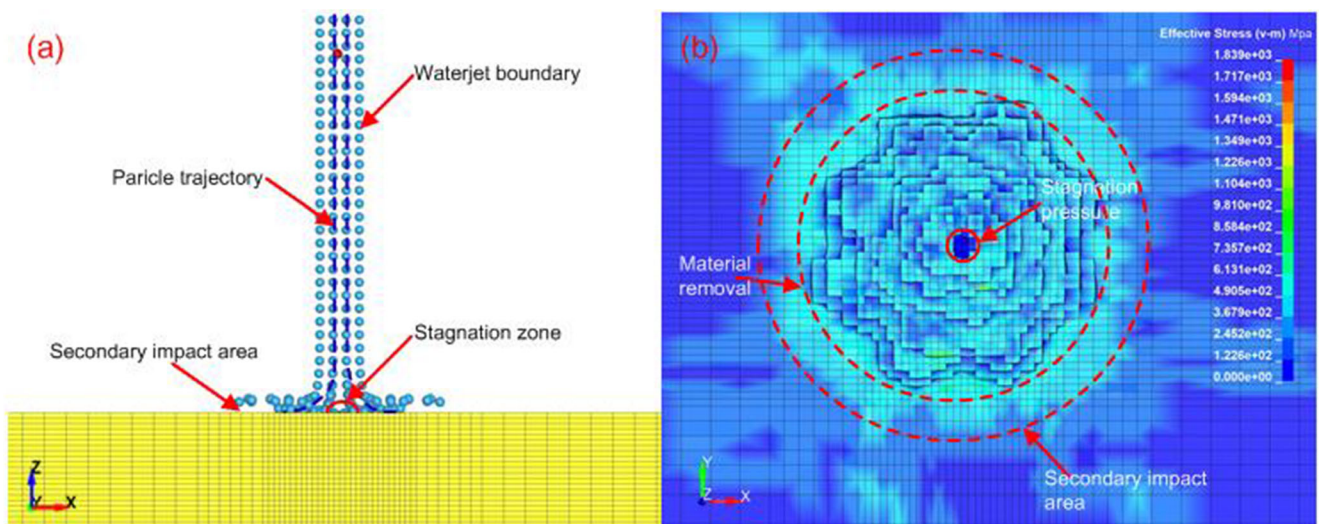
Fig. 11 Simulation results of the impact pressure variation along the workpiece surface: **a** particle trajectory and stagnation zone; **b** effective pressure distribution

rate, abrasive size, impact angle, etc. easy to adjust. Therefore, the discussion part will take advantage of the numerical model to discuss the effect of abrasive parameters on the cutting quality.

Figure 14 illustrates the influence of abrasive mass flow rate $\dot{m}_a$ on kerf characteristics. It can be seen that the depth

of cut and kerf top width increases when the abrasive mass flow rate $\dot{m}_a$ rises from 0 kg/min to 0.18 kg/min, but the kerf top width changes more slightly. This is attributed to the fact that when the abrasive mass flow rate is increased, more abrasives impact per unit area of the target. Thus, the cutting depth is increased.

Fig. 12 Measurements of the crater in AWJ experiments: **a** 3D-scanned surface; **b** 2D profile of the centric cross-sectional view
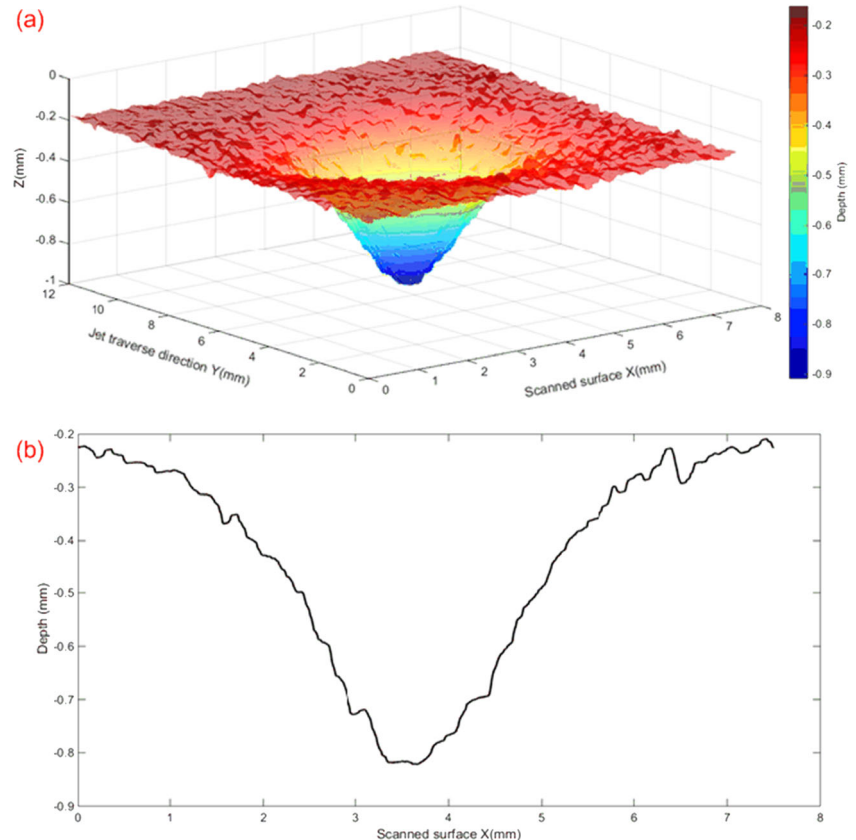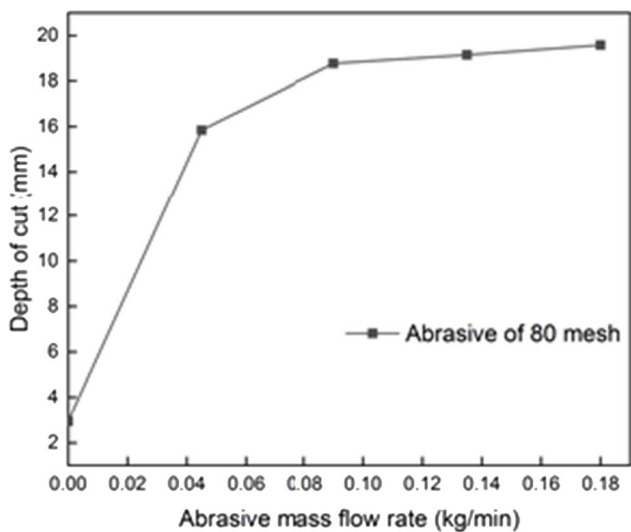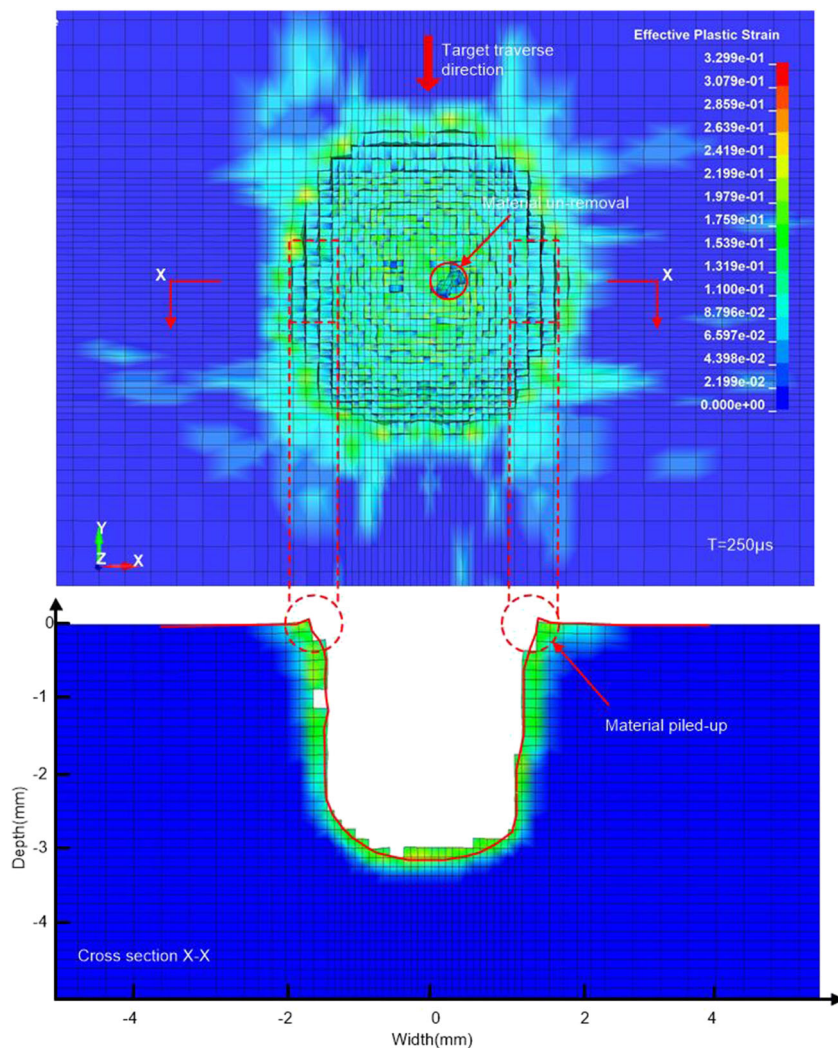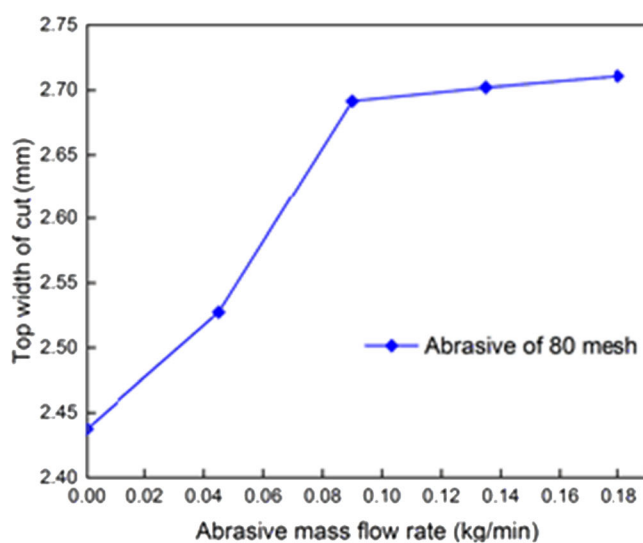
Fig. 13 Details of piled-up
material at the cutting edge area

Fig. 14 Effect of abrasive mass flow rate on kerf characteristics: **a** cutting depth; **b** kerf top width
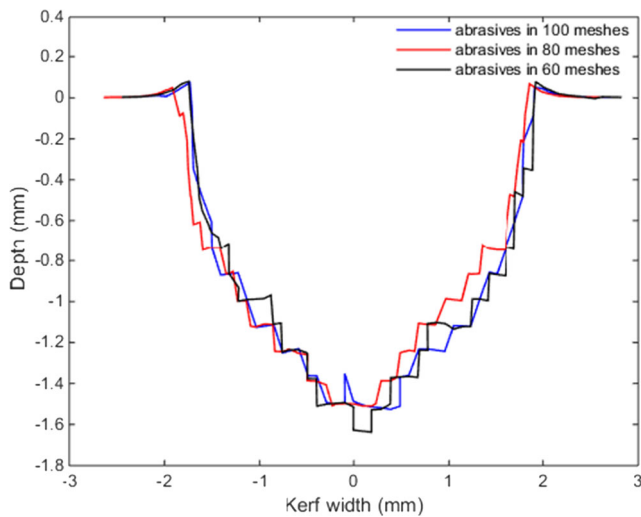
Fig. 15 Effect of abrasive size on kerf characteristics

the jet impact angles. It can be observed from Fig. 16a that the kerf shape is symmetric when the impingement angle is 90. But when the impingement angle decreases, the shape of kerf becomes asymmetric. One side of the impacted wall is gradually vertical, as presented in Fig. 16b–c. The conclusions can be used to instruct the kinematic parameters selecting in AWJ machining.

6 Conclusions

In this paper, the coupled SPH-DEM-FEM modeling method is proposed to simulate the abrasive water jet machining process. The newly developed AWJ modeling method is capable to reproduce the actual high-speed response of the workpiece by incorporating SPH, DEM, and FEM in a single numerical model. Based on the current work, the following conclusions can be obtained.

As demonstrated in Fig. 15, there is no significant improvement in the cut depth and kerf top width, while the size of abrasive particles increases from 0.147 to 0.25 mm (mesh 100, 80, 60). This is because the cutting depth is dominated by the parameters as water pressure, jet traverse speed, and abrasive mass flow rate, which have significant contributions to jet energy. And the kerf top width is sensitive to the effective jet width that is mainly determined by the standoff distance.

Figure 16 shows the effect of jet impact angle on the kerf geometry, where α is the impingement angle and β represents the angle of the kerf shape change. It can be seen that the jet cutting depth decreases slightly as the tilt angle is increasing, which is due to the fact that more effective impacts occur on the kerf wall other than the bottom. On the contrary, the kerf shape is sensitive to

(1) The automatic generation method of abrasive particles and water flow is adopted in the model, which enables the long-time AWJ simulating of thick plates and improves the calculation efficiency significantly.

(2) A further understanding of the kerf formation process is provided. The pressure stagnation zone is proved to be formed in the middle part of the waterjet, which prevents the material in the central impacted area from erosion. And the material is piled up on the kerf boundaries owing to the strikes of particles on the kerf walls.

(3) The abrasive particles are characterized by DEM, which significantly simplifies the modeling difficulty of abrasive particles. The influence of abrasive parameters such as the mass flow rate, irregular geometry, and the particle size distribution is investigated.
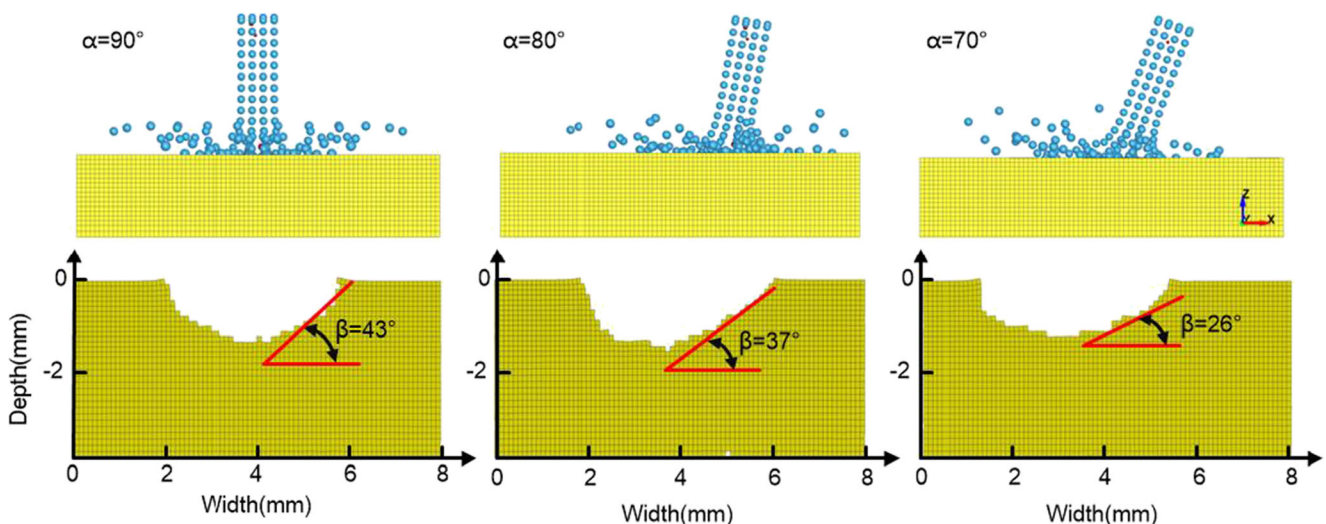

Fig. 16 Effect of impacting angle on kerf characteristics

References

1. Liu HT (2017) Precision machining of advanced materials with waterjets. IOP Conf Ser Mater Sci Eng 164:012008. https://doi.org/10.1088/1757-899x/164/1/012008

2. Wang F, Ji K, Guo Z (2020) Microstructural analysis of failure progression for coated carbide tools during high-speed milling of Ti-6Al-4V. Wear 456-457:203356. https://doi.org/10.1016/j.wear.2020.203356

3. Liu X, Liang Z, Wen G, Yuan X (2019) Waterjet machining and research developments: a review. Int J Adv Manuf Technol 102:1257–1335. https://doi.org/10.1007/s00170-018-3094-3

4. Li X, Ruan X, Zou J, Long X, Chen Z (2020) Experiment on carbon fiber–reinforced plastic cutting by abrasive waterjet with specific emphasis on surface morphology. Int J Adv Manuf Technol 107(1–2):145–156. https://doi.org/10.1007/s00170-020-05053-y

5. Hashish M (1991) Optimization factors in abrasive-waterjet machining. J Eng Ind 113(1):29–37

6. Hlavacova IM, Geryk V (2017) Abrasives for waterjet cutting of high-strength and thick hard materials. Int J Adv Manuf Technol 90(5):1217–1224. https://doi.org/10.1007/s00170-016-9462-y

7. Yu Y, Sun T, Yuan Y, Gao H, Wang X (2020) Experimental investigation into the effect of abrasive process parameters on the cutting performance for abrasive waterjet technology: a case study. Int J Adv Manuf Technol 107(5–6):2757–2765. https://doi.org/10.1007/s00170-020-05183-3

8. Lebar A, Junkar M (2004) Simulation of abrasive water jet cutting process: part 1. Unit event approach. Model Simul Mater Sci Eng 12(6):1159–1170

9. Liang Z, Xie B, Liao S, Zhou J (2015) Concentration degree prediction of AWJ grinding effectiveness based on turbulence characteristics and the improved ANFIS. Int J Adv Manuf Technol 80(5–8):887–905. https://doi.org/10.1007/s00170-015-7027-0

10. Lv Z, Hou R, Chen X, Huang C (2019) Numerical research on erosion involved in ultrasonic-assisted abrasive waterjet machining. Int J Adv Manuf Technol 103:617–630. https://doi.org/10.1007/s00170-019-03584-7

11. Feng L, Liu GR, Li Z, Dong X, Du M (2018) Study on the effects of abrasive particle shape on the cutting performance of Ti-6Al-4V materials based on the SPH method. Int J Adv Manuf Technol 101(9–12):3167–3182. https://doi.org/10.1007/s00170-018-3119-y

12. Pozzetti G, Peters B (2018) A numerical approach for the evaluation of particle-induced erosion in an abrasive waterjet focusing tube. Powder Technol 333:229–242. https://doi.org/10.1016/j.powtec.2018.04.006

13. Qiang Z, Wu M, Miao X, Sawhney R (2018) CFD research on particle movement and nozzle wear in the abrasive water jet cutting head. Int J Adv Manuf Technol 95(9–12):4091–4100. https://doi.org/10.1007/s00170-017-1504-6

14. Nyaboro JN, Ahmed MA, El-Hofy H, El-Hofy M (2018) Numerical and experimental characterization of kerf formation in abrasive waterjet machining. In: ASME International Mechanical Engineering Congress and Exposition, vol 52019. American Society of Mechanical Engineers, p V002T02A050. https://doi.org/10.1115/IMECE2018-88617

15. Liu H, Wang J, Kelson N, Brown RJ (2004) A study of abrasive waterjet characteristics by CFD simulation. J Mater Process Technol 153-154:488–493. https://doi.org/10.1016/j.jmatprotec.2004.04.037

16. Eltobgy MS, Ng E, Elbestawi MA (2005) Finite element modeling of erosive wear. Int J Mach Tools Manuf 45(11):1337–1346. https://doi.org/10.1016/j.ijmachtools.2005.01.007

17. Anwar S, Axinte DA, Becker AA (2013) Finite element modelling of abrasive waterjet milled footprints. J Mater Process Technol 213(2):180–193. https://doi.org/10.1016/j.jmatprotec.2012.09.006

18. Jianming W, Na G, Wenjun G (2010) Abrasive waterjet machining simulation by SPH method. Int J Adv Manuf Technol 50(1–4):227–234. https://doi.org/10.1007/s00170-010-2521-x

19. Feng Y, Jianming W, Feihong L (2011) Numerical simulation of single particle acceleration process by SPH coupled FEM for abrasive waterjet cutting. Int J Adv Manuf Technol 59(1–4):193–200. https://doi.org/10.1007/s00170-011-3495-z

20. Wenjun G, Jianming W, Na G (2010) Numerical simulation for abrasive water jet machining based on ALE algorithm. Int J Adv Manuf Technol 53(1–4):247–253. https://doi.org/10.1007/s00170-010-2836-7

21. Anwar S, Axinte DA, Becker AA (2013) Finite element modelling of overlapping abrasive waterjet milled footprints. Wear 303(1–2):426–436. https://doi.org/10.1016/j.wear.2013.03.018

22. Lozano Torrubia P, Axinte DA, Billingham J (2015) Stochastic modelling of abrasive waterjet footprints using finite element analysis. Int J Mach Tools Manuf 95:39–51. https://doi.org/10.1016/j.ijmachtools.2015.05.001

23. Dong X, Li Z, Jiang C, Liu Y (2019) Smoothed particle hydrodynamics (SPH) simulation of impinging jet flows containing abrasive rigid bodies. Comput Part Mech 6(3):479–501

24. Xu J, Wang J (2013) Node to node contacts for SPH applied to multiple fluids with large density ratio. In: Proceedings of the 9th European LS-DYNA Users' Conference, Manchester, UK, pp 2–4

25. Yreux E (2018) Fluid flow modeling with SPH in LS-DYNA®. In: Proceedings of the 15th International LS_DYNA Users Conference, Dearborn, MI, USA

26. Flores-Johnson EA, Wang S, Maggi F, El Zein A, Gan Y, Nguyen GD, Shen L (2016) Discrete element simulation of dynamic behaviour of partially saturated sand. Int J Mech Mater Des 12(4):495–507. https://doi.org/10.1007/s10999-016-9350-5

27. Karajan N, Han Z, Teng H, Wang J (2014) On the parameter estimation for the discrete-element method in LS-DYNA®. In: Proceedings of the 13th International LS_DYNA Users Conference, Dearborn, MI, USA, pp 8–10

28. Karajan N, Han Z, Ten H, Wang J (2013) Interaction possibilities of bonded and loose particles in LS-DYNA. In: Proceedings of the 9th European LS-DYNA Users' Conference, Manchester, UK, no 1, pp 1–27

29. LSTC (2019) LS-DYNA keyword user's manual, vol I. Livemore Software Technology Corporation, Livermore

30. Tokura S (2015) Validation of fluid analysis capabilities in LS-DYNA Based on experimental eesult. In: Proceedings of the 10th European LS-DYNA Users' Conference, Würzburg

31. Wang F, Wang R, Zhou W, Chen G (2017) Numerical simulation and experimental verification of the rock damage field under particle water jet impacting. Int J Impact Eng 102:169–179. https://doi.org/10.1016/j.ijimpeng.2016.12.019

32. Johnson GR, Cook WH (1985) Fracture characteristics of three metals subjected to various strains, strain rates, temperatures and pressures. Eng Fract Mech 21(1):31–48. https://doi.org/10.1016/0013-7944(85)90052-9

33. Crocker L (2017) Good practice guide to the application of finite element analysis to erosion modelling. National Physical Laboratory, Teddington

34. Momber AW, Kovacevic R (2012) Principles of abrasive water jet machining. Springer Science & Business Media, London

35. Eitobgy M, Ng EG, Elbestawi MA (2005) Modelling of abrasive waterjet machining: a new approach. CIRP Ann 54(1):285–288. https://doi.org/10.1016/s0007-8506(07)60104-8

36. Chen FL, Siores E (2001) The effect of cutting jet variation on striation formation in abrasive water jet cutting. Int J Mach Tools Manuf 41(10):1479–1486. https://doi.org/10.1016/S0890-6955(01)00013-X

37. Schwartzentruber J, Spelt JK, Papini M (2018) Modelling of delamination due to hydraulic shock when piercing anisotropic carbon-fiber laminates using an abrasive waterjet. Int J Mach Tools Manuf 132:81–95. https://doi.org/10.1016/j.ijmachtools.2018.05.001